

# An Analysis of the Effect of the Zirconium Precursor of MOF-808 on its Thermal Stability and Structural and Surface Properties

C. Ardila-Suárez<sup>1,2</sup>, J. Rodríguez-Pereira<sup>2,3</sup>, Víctor G. Baldovino-Medrano<sup>1,2,3</sup>, and G.E. Ramírez-Caballero<sup>1,2\*</sup>

<sup>1</sup>Grupo de Investigación en Polímeros, <sup>2</sup>Centro de Investigaciones en Catálisis ([@CICATUIS](#)), and <sup>3</sup>Laboratorio de Ciencia de Superficies ([@Csss-UIS](#)), all at Parque Tecnológico de Guatiguará (PTG), km 2 vía El Refugio, Universidad Industrial de Santander, Piedecuesta (Santander), 681011, Colombia

[\\*gusramca@uis.edu.co](mailto:gusramca@uis.edu.co)

## Table of Contents

1.	Experimental Methods .....	2
1.1.	Crystallinity.....	2
1.2.	Porosity Calculations.....	2
1.3.	Surface Chemistry .....	2
2.	Results and Discussion .....	6
2.1.	Thermal Stability .....	6
2.2.	Crystallinity.....	7
2.3.	Surface Area and Porosity .....	11
2.3.1.	BET- Rouquerol Consistency Criteria .....	11
2.3.2.	Considerations of the $\chi$ - Method .....	13
2.3.3.	Pore Size Distributions and Pore Volume .....	14
2.4.	Surface Chemistry .....	16
	Supplementary References .....	20

## 1. Experimental Methods

### 1.1. Crystallinity

The indexation of the powder diffraction patterns was performed with the Dicvol06 program, and the structures were solved through Le Bail analysis both using the FullProf software. Also, an estimate of the relative crystallinity between the synthesized materials was performed by the analysis of the integrated intensity areas of the characteristic XRD diffraction peaks of MOF-808 (ZrBTC MOF) ( $2\theta = 4.33^\circ, 7.14^\circ, 8.32^\circ, 8.69^\circ, 10^\circ, 10.9^\circ, 13^\circ, 14.2^\circ$  and  $19.32^\circ$ ), using the OriginPro software after baseline correction following a procedure reported elsewhere [1].

### 1.2. Porosity Calculations

Microporous pore size distributions were calculated using the Ar recorded isotherms via a Non-Local Density Functional Theory (NLDFT) routine with a model isotherm for oxides with cylindrical pores as in agreement with previous literature proposals [2, 3]. A regularization factor of 0.0316 was employed. Mesoporous pore size distributions were calculated by the Barret-Joyner-Halenda (BJH) method [4] assuming cylindrical pores. Cumulative pore volumes were calculated from the NLDFT routine. The calculation routines were provided in the *MicroActive* Micromeritics software of the instrument.

### 1.3. Surface Chemistry

Analyses were performed on the A. Centeno-XPS/ISS/UPS surface characterization platform built by SPECS. The platform is provided with a PHOIBOS 150 2D-DLD energy analyzer package. A monochromatized Al  $K\alpha$  X-ray source (Focus 500) operated at 200 W was employed. The pressure in the analysis chamber was approximately  $1 \times 10^{-7}$  Pa. The angle between the normal to the sample surface and the direction of photoelectrons collection

was about 54°. Samples were mounted on carbon conductive tape over metallic sample holders for analysis. Surface charge compensation was controlled with a flood gun (FG 15/40-PS FG500 device) operated at 58  $\mu\text{A}$  and 1.0 eV. Spectra were collected in the Fixed Analyzer Transmission mode. The spot area for analyses was  $3.5 \times 1.0 \text{ mm}^2$ . The pass energy of the hemispherical analyzer was set at 100 eV for general spectra and to 60 eV for high-resolution spectra. The energy step for acquisition was set to 0.050 eV. General spectra were recorded first for all samples followed by high-resolution spectra. The C 1s peak was recorded both at the beginning and at the end of the measurements for checking the evolution of surface charge during the analyses. High resolution spectra were recorded following elements identification in the general spectra and according to samples chemistry and history. Data analysis was performed with the CasaXPS program (Casa Software Ltd) using the SPECS Prodigy library for R.S.F. values. A U 3 Tougaard baseline [5] was employed for background modeling together with a Lorentzian line shape, LA(1.53,243) in CasaXPS, for peak decomposition. For the C 1s peak, the following chemical species, ordered from lower to higher binding energies (BEs), were considered: (i) Carbon belonging to an aromatic ring, labeled as C-Ar. Under the analysis conditions employed herein, this component is indistinguishable from the peak from the C-(C,H) species from aliphatic hydrocarbons. In consequence, a single component centered at 284.8 eV [6] was assumed for both species. This component was employed as a reference for correcting the BE scale of the spectra. (ii) Carbon from the carboxylic acid group linked to the Zr cluster, labeled as Ar-(C-O)-Zr. For the analyzed samples, the mean BE for this component was within the 95.0 % confidence interval (t-Student, 2 degrees of freedom)  $-C.I._{t,0.05;2}$  for the mean = [285.9, 286.3] eV-. (iii) Carbon

belonging to the carboxylic acid group of H<sub>3</sub>BTC, labeled as Ar-Carboxy. Based on literature references [6, 7], the peak for this component was fixed at 288.0 eV. (iv) Carbon from the carboxylic acid group linked to an aliphatic chain, labeled as Aliph-Carboxy and fixed at 289.0 eV [7]. An additional peak corresponding to the  $\pi - \pi^*$  from the aromatic ring was considered for peak decomposition [8]. The C.I.<sub>±0.05;2</sub> mean BE for this component was within the range: [290.6, 291.4] eV. For this component, the R.S.F. value was set to 0 during chemical species quantification. The same FWHM for set for all carbon species and for the  $\pi - \pi^*$  transition peak. For the O 1s peak, three species were considered. The first was oxygen linked to Zr in the inorganic cluster, labeled O-Zr; C.I.<sub>±0.05;2</sub> for the mean = [530.4, 531.0] eV. The second was oxygen belonging to a carboxylic acid functional group; C.I.<sub>±0.05;2</sub> for the mean = [531.9, 532.4] eV. In the O 1s peak, this component, labelled as R-(C=O)-OH, cannot be further decomposed into carboxylates linked to an aromatic or aliphatic chain [6]. The third oxygen component; C.I.<sub>±0.05;2</sub> for the mean = [533.6, 534.1] eV, was ascribed to oxygen belonging to the Zr-O-C bonds in the MOF. This proposal is coherent with the BE shifts expected when comparing the parent carbon components described before, in the sense that if the corresponding carbon is more oxidized, the oxygen must be more reduced. No constraints were imposed during peak decomposition except for assuming the same FWHM for all components. Finally, for the Zr 3d peak, two species were considered. The first was Zr coordinated to an organic group through oxygen, labeled Zr-O-C; C.I.<sub>±0.05;2</sub> for the mean of the Zr 3d<sub>5/2</sub> peak = [182.0, 182.5] eV, and the second Zr belonging to inorganic clusters; C.I.<sub>±0.05;2</sub> for the mean of the Zr 3d<sub>5/2</sub> peak = [182.7, 183.0], labeled Zr-O. The above BE assignment was also made considering the relative BE shifts expected from the

corresponding oxygen and carbon components. The following constraints were imposed during peak decomposition: a) the area of the Zr 3d<sub>3/2</sub> core level is equal to two thirds of the area of the Zr 3d<sub>5/2</sub> core level, and, b) a separation of 2.37 eV between both core levels was assumed [9]. In addition, four components corresponding to overlapping loss features from the Zr 3d core levels of each assigned species were considered for peak decomposition but not accounted for in quantification; i.e. R.S.F. fixed to 0. The chemical structures used for peak decomposition are illustrated in Figure S1.

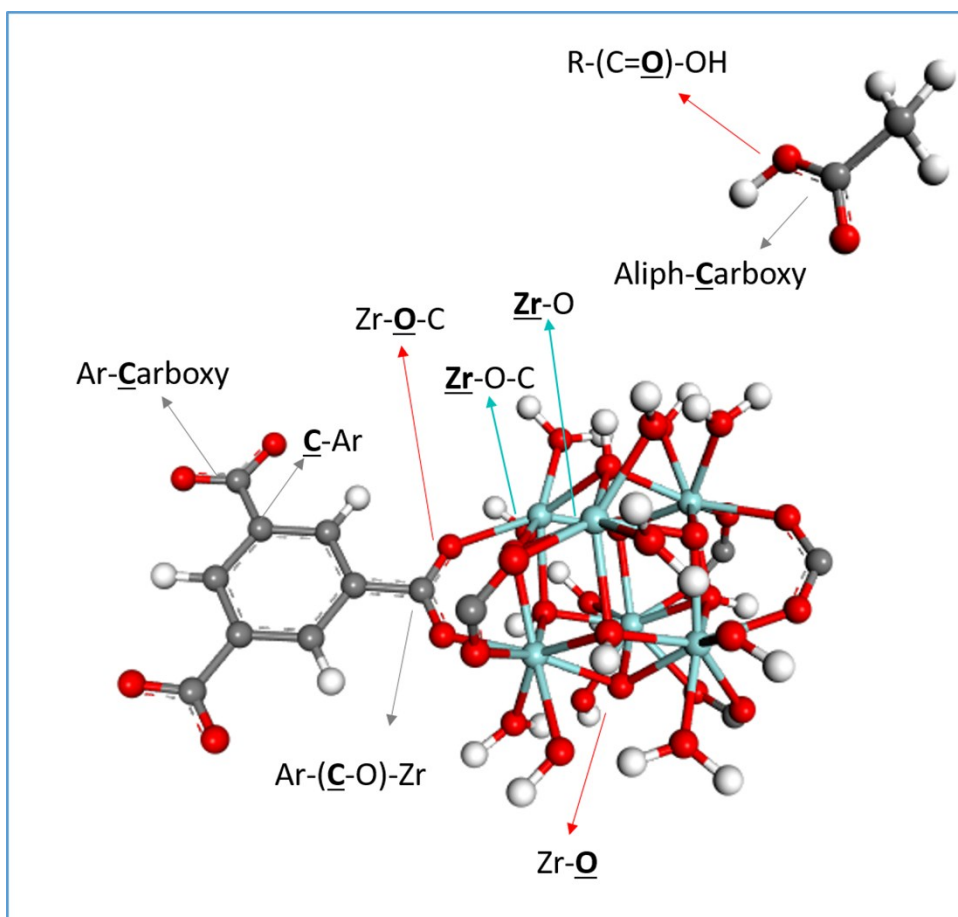


**Figure S1.** Schematic representation of the proposed surface chemical species of C 1s, O 1s and Zr 3d peaks for the synthesized materials.

## 2. Results and Discussion

### 2.1. Thermal Stability

The thermal profiles of all materials were similar. In region I, relative weight losses decreased in the order: ZrBTC1 (~28.1%) > ZrBTC2 (~25.7%) > ZrBTC1 (~23.9%). One may notice that this trend resembles the one obtained for the surface areas; see section 3.2. In region II, weight losses followed the trend: ZrBTC3 (~11.7%) > ZrBTC2 (~10.4%) > ZrBTC1 (~10.2%). Finally, in region III, the trend was: ZrBTC3 (~29.4%) > ZrBTC1 (~27.4%) > ZrBTC2 (~26.6%). Finally, under the assumption that there is a complete combustion of the organic components of the material under the air atmosphere at the end of the thermogram, the materials are converted to  $ZrO_2$ , the following percentages of  $ZrO_2$  were calculated: ZrBTC2 = 37.3 %, ZrBTC3 = 35.0 %, and ZrBTC1 = 34.3 %. Accordingly, the relative percentages of zirconium of the synthesized materials were: 27.6% for ZrBTC2, 25.9 % for ZrBTC3, and 25.4 % for ZrBTC1.

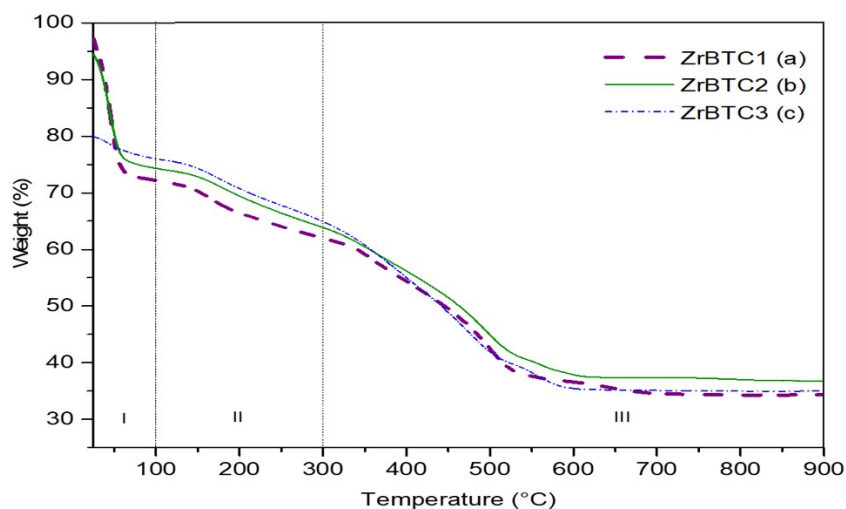


**Figure S2.** Thermogravimetric analysis (TGA) in air atmosphere of ZrBTC MOFs from precursors: (a)  $ZrCl_4$  (ZrBTC1), (b)  $ZrOCl_2 \cdot 8H_2O$  (ZrBTC2) and (c)  $ZrO(NO_3)_2 \cdot xH_2O$  (ZrBTC3).

## 2.2. Crystallinity

**Table S1.** Indexation of the powder diffraction pattern of ZrBTC1 material synthesized from  $ZrCl_4$  precursor, using DICVOL06 program at Fullprof Software.

hkl index	2 theta	hkl index	2 theta	hkl index	2 theta
1 1 1	4.3443	10 4 2	27.7395	15 3 1	39.2008
2 2 0	7.0971	7 7 5	28.0911	14 6 2	39.2876
3 1 1	8.3241	11 1 1	28.0911	13 7 5	39.8903
2 2 2	8.6949	8 8 0	28.6683	12 8 6	39.9758
4 0 0	10.0432	9 7 1	29.0096	14 6 4	40.3163
3 3 1	10.947	8 8 2	29.1226	13 9 1	40.57
4 2 2	12.3083	8 6 6	29.5704	16 0 0	40.9901
3 3 3	13.0581	11 3 3	29.9023	13 9 3	41.2404
4 4 0	14.2216	10 6 2	30.0122	12 10 4	41.3236
5 3 1	14.8769	12 0 0	30.4482	16 2 2	41.6549
4 4 2	15.0891	11 5 1	30.7715	11 11 5	41.902
6 2 0	15.9105	12 2 2	31.3036	14 6 6	41.9841
5 3 3	16.5004	9 7 5	31.619	12 8 8	42.3112
6 2 2	16.6925	12 4 0	32.1385	15 5 5	42.5552
4 4 4	17.4404	9 9 1	32.4467	16 4 2	42.6363
7 1 1	17.9815	12 4 2	32.5488	12 10 6	42.9593
6 4 2	18.85	10 8 2	32.9545	15 7 3	43.2003
7 3 1	19.3531	13 1 1	33.2559	16 4 4	43.5997
8 0 0	20.1647	12 4 4	33.753	17 1 1	43.8379
7 3 3	20.6369	13 3 1	34.0481	12 12 2	43.917
6 4 4	20.7921	10 8 4	34.146	16 6 2	44.2326
8 2 2	21.4019	12 6 2	34.5351	15 7 5	44.4681
7 5 1	21.8486	13 3 3	34.8244	14 10 2	44.5463
6 6 2	21.9955	8 8 8	35.302	12 12 4	44.8584
8 4 0	22.5743	11 7 5	35.5859	17 3 3	45.0913
9 1 1	22.9994	12 6 4	35.6801	12 10 8	45.1687
8 4 2	23.1394	14 2 0	36.0547	14 10 4	45.4774
6 6 4	23.6918	13 5 3	36.3335	13 11 5	45.7078
9 3 1	24.0982	14 2 2	36.426	16 8 0	46.0899
8 4 4	24.7616	12 8 0	36.794	15 7 7	46.318
7 7 1	25.1517	11 9 3	37.068	14 8 8	46.3938
8 6 2	25.7897	12 8 2	37.159	18 2 0	46.6962
7 7 3	26.1655	12 6 6	37.5208	13 9 9	46.922
9 5 1	26.1655	13 5 5	37.7903	18 2 2	46.997
6 6 6	26.2897	12 8 4	38.2358	16 8 4	47.2965
10 2 2	26.2897	13 7 3	38.501	13 13 1	47.5201
9 5 3	27.1441	14 4 4	38.5891	18 4 2	47.891
8 6 4	27.2641	14 6 0	38.9397	13 13 3	48.1125

**Table S2.** Crystallinity data and structure refinement of the ZrBTC1, ZrBTC2, and ZrBTC3 materials, synthesized from  $ZrCl_4$ ,  $ZrOCl_2 \cdot 8H_2O$ , and,  $ZrO(NO_3)_2 \cdot xH_2O$  precursors, respectively.

	ZrBTC1	ZrBTC2	ZrBTC3
Crystal system	Cubic	Cubic	Cubic
Space group	$Fd\bar{3}m$	$Fd\bar{3}m$	$Fd\bar{3}m$
Cell parameters	35.2039(48)	34.8548(143)	34.5580(674)
Volume	43628.660(3.99)	42343.605(20.320)	41270.965(49.210)
Chi2	1.73	1.32	1.82

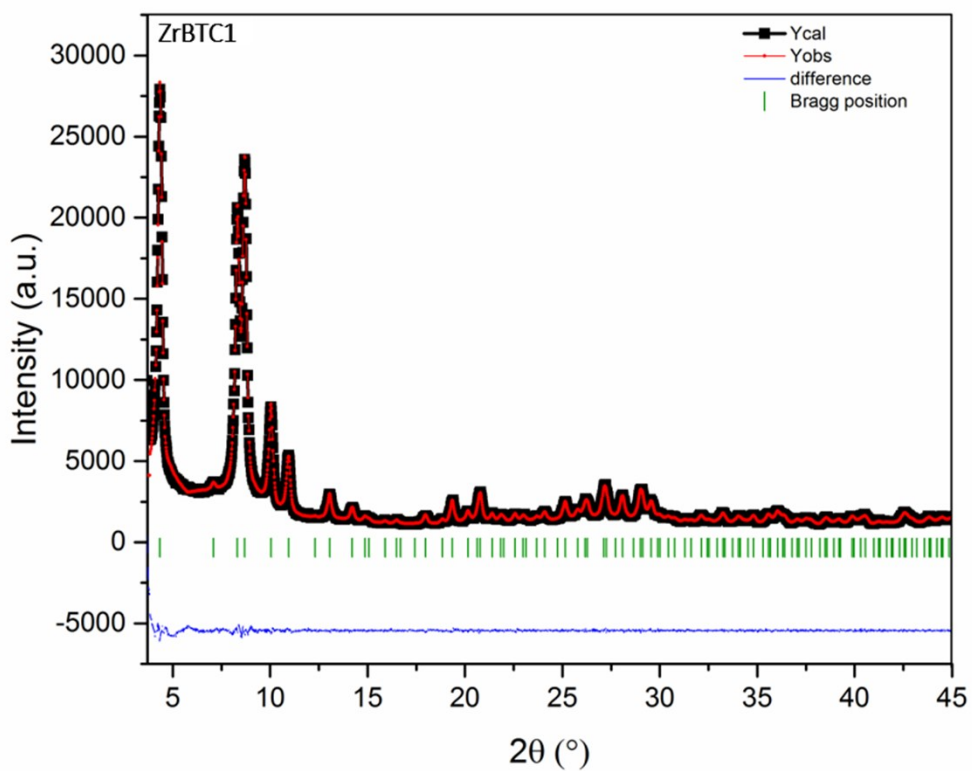


**Figure S3.** Le Bail profile fitting for ZrBTC1 synthesized from  $ZrCl_4$  precursor using experimental PXRD data. Experimental data is shown in red squares, the calculation in black, difference in blue line, and Bragg reflection markers in green.

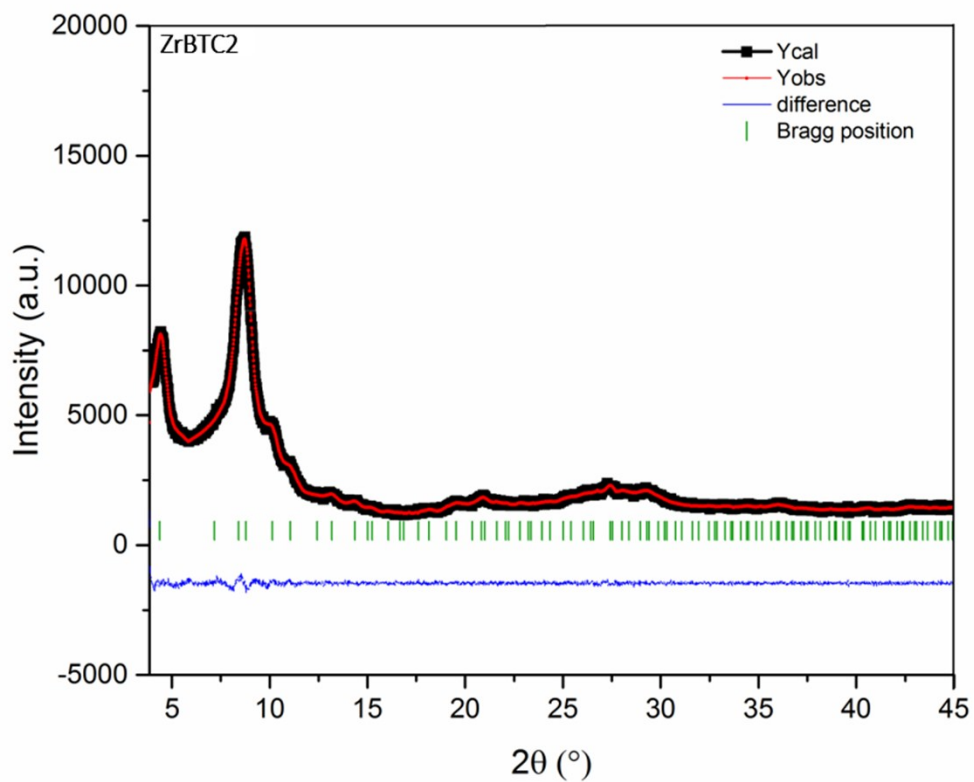


**Figure S4.** Le Bail profile fitting for ZrBTC2 synthesized from  $ZrOCl_2 \cdot 8H_2O$  precursor using experimental PXRD data. Experimental data is shown in red squares, the calculation in black, difference in blue line, and Bragg reflection markers in green.

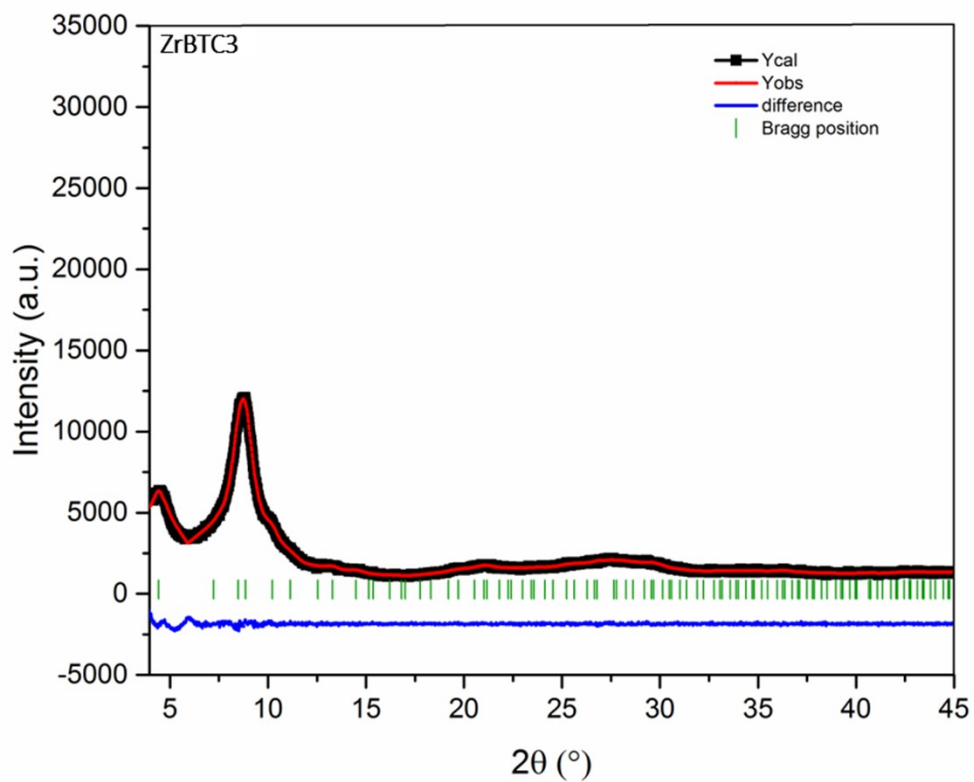


**Figure S5.** Le Bail profile fitting for ZrBTC3 synthesized from  $ZrO(NO_3)_2 \cdot xH_2O$  precursor using experimental PXRD data. Experimental data is shown in red squares, the calculation in black, difference in blue line, and Bragg reflection markers in green.

## 2.3. Surface Area and Porosity

### 2.3.1. BET- Rouquerol Consistency Criteria

Rouquerol et al [10] proposed that the following conditions must be met for choosing an appropriate  $P/P_0$  range for surface area calculation: (1) In a plot of  $n(1 - P/P_0)$  vs  $P/P_0$ , one should select only those experimental points where the former increases monotonically. (2) The value of the BET constant  $C$  estimated from the linear regression of the BET transform plot should be positive. (3) The amount of the adsorbed gas probe calculated for the BET statistical monolayer; i.e. the BET monolayer capacity ( $n_m$ ), must be within the range of selected  $P/P_0$ . And, (4) the relative pressure corresponding to the BET monolayer capacity should be approximately equal to  $(1/((C)^{1/2}+1))$ . They also suggested that the points select for estimating the surface must conform to a linear adjustment. Table S3 shows the calculated  $SA_{\text{BET}}$  for the synthesized materials and the compliance of the above criteria found for these calculations. According to results,  $SA_{\text{BET}}$  followed the trend: ZrBTC1 ( $SA_{\text{BET}} = 1068 \text{ m}^2/\text{g}$ ) > ZrBTC2 ( $SA_{\text{BET}} = 764 \text{ m}^2/\text{g}$ ) > ZrBTC3 ( $SA_{\text{BET}} = 552 \text{ m}^2/\text{g}$ ). In general, the four consistency criteria commented above were met except for the linear fitting criterion established by the software. The latter is due to the fact that the isotherms presented changes in their slopes within the  $P/P_0$  region where micropores are found. Such a feature is not encountered on other microporous materials such as the zeolites that Rouquerol et al. [10] studied. Therefore, even when the consistency criteria other than the linear fitting criterion were met, the microporous structure of the ZrBTC MOFs synthesized herein does not allow for a rigorous quantitative assessment of surface area via the BET method; not

even if the calculated surface areas are said to be apparent surface areas [10]. This does not invalidate the qualitative trend found for the effect of the change of Zr precursor on surface area though. In this sense, calculated  $SA_{BET}$  values evidenced that the use of  $ZrOCl_2 \cdot 8H_2O$  and  $ZrO(NO_3)_2 \cdot xH_2O$  produced materials with lower surface areas as compared to  $ZrCl_4$ .

**Table S3.** Comparison of the apparent surface areas calculated using BET method taking into account the full consistency criteria proposed by Rouquerol of the ZrBTC1, ZrBTC2 and, ZrBTC3 materials, synthesized from  $ZrCl_4$ ,  $ZrOCl_2 \cdot 8H_2O$ , and,  $ZrO(NO_3)_2 \cdot xH_2O$  precursors, respectively.

BET - Rouquerol Consistency Criteria						
Sample	SA (m <sup>2</sup> /g)	C value > 0	n(min) < monolayer < n(max)	P/Po(mono) ~1/(√C+1)	Linear fitting R <sup>2</sup>	Rsq
ZrBTC1	1068	True- 89.08	True	True	False	0.89536
ZrBTC2	764	True- 112.7	True	True	False	0.97406
ZrBTC3	552	True-101.64	True	True	False	0.98441

### 2.3.2. Considerations of the $\chi$ - Method [11]

The equation for the  $\chi$ - theory is:

$$\frac{nfA_m}{A_s} = -\ln\left[-\ln\left(\frac{P}{P_s}\right)\right] - \ln\left(-\frac{E_a}{RT}\right)$$

Then, in the transformed equation  $y = n_{ad}$  and  $x = -\ln\left[-\ln\left(\frac{P}{P_s}\right)\right]$ .

Where the slope and the intercept are, respectively:  $S_i = \frac{A_s}{fA_m}$  and  $I_i = S_i\left[-\ln\left(\frac{E_a}{RT}\right)\right]$

The surface area is calculated using a value of 1.84 for  $f$  and determining the value of  $A_m$  (the molar area) from

$$A_m = (V_m)^{2/3}(N_A)^{1/3}$$

Where  $V_m$  is the molar volume and  $N_A$  is the Avogadro's number. The value of  $A_m$  for argon is  $7.90 \times 10^4 \text{ m}^2 \text{ mol}^{-1}$  at its normal boiling point.

If several segments are observed in the isotherm, the surface areas for each segment,

$A_{s,i}$  is given by

$A_{s,i} = 1.84A_m(S_i - S_{i-1})$ , where  $S_0 = 0$ . Also, the Energy of adsorption of each segment is

given by:

$$E_{a,i} = -RT \exp\left(-\frac{I_i}{S_i}\right)$$

For the mesoporous range, 
$$S_{hi} = \frac{A_{ex}}{fA_m}$$

Also, it necessary to determine the value of  $\chi_c = -\frac{I_{lo}}{S_{lo}}$ , where  $I_{lo}$  is the intercept of the low-pressure linear portion. Then, the pore volume is:

$$V_p = V_m(S_{hi}\chi_c + I_{hi})$$

The theory is characterized by the fact that it is possible to consider several surfaces with different energies of adsorption for the calculation of the total surface area. Surface area assessment by the  $\chi$ -method follows from a rather simple transformation of the physisorption isotherm; i.e. the  $\chi$ -plot in Figures 2d to 2f. According to Condon [11], regardless of the isotherm type, the section of a  $\chi$ -plot found at lower relative pressures is associated to the interaction of the probe molecule with the highest surface energy. For MOFs studied herein, such section belongs relative pressures below ca.  $P/P_0 = 0.1$  where micropores are accessed by argon. One may observe in Figures 2d to 2f an initial linear section for the constructed  $\chi$ -plots. Such a section would thus correspond to argon accessing the smallest pores; i.e. micropores, of the materials. Upward bendings of the isotherm may be interpreted as the probe molecules in the gas phase increasing the frequency of their interactions with other adsorbed probe molecules instead of solely adsorbing on the bare surface of the solid. When a further linear section appears in the  $\chi$ -plot it implies that the probe molecule is now mostly interacting with a surface of the solid that is more open hence

with lower surface energy. Every linear portion of the  $\chi$ -plot is considered to correspond to a surface with a characteristic average surface energy hence resulting in a distribution of surface energies. Such energy distribution is associated to a distribution of surface areas in the  $\chi$ -theory and related methods using standard plots [11-14]. In general, the total surface area is considered to be a linear summation of the surface areas of each of the surfaces of the solid displaying a similar surface energy. Hence, the application of the  $\chi$ - method is sensitive to the presence of different distributions of micropores and mesopores in a studied material; which is the case of the MOFs synthesized in this work.

### 2.3.3. Pore Size Distributions and Pore Volume

All Materials displayed multiple families of pores whose presence led to stepped cumulative pore volume curves. In the case of ZrBTC1, a total pore volume of 0.61 cm<sup>3</sup>/g was estimated. According to calculations, 15.7 % of this volume corresponds to pores with an average size of ca. 0.6 nm, 42.8% corresponds to pores with an average size of ca. 1.5 nm, and 41.5 % corresponds to pores with an average size of ca. 28 nm. The two families of micropores described above displayed relatively narrow ranges of pore sizes. Conversely, the family of mesopores had a wide range of sizes spanning from 10 to 50 nm. For ZrBTC2, the cumulative pore volume amounted to 0.43 cm<sup>3</sup>/g; *ergo*, a 40% decrease in pore volume was obtained by using ZrOCl<sub>2</sub>•8H<sub>2</sub>O as metallic precursors instead of ZrCl<sub>4</sub>. As in the case of ZrBTC1, two families of micropores with average sizes of 0.6 and 1.5 nm were also found for ZrBTC2. Conversely, calculations indicated the existence of one additional family of micropores with an average size around ca. 1.0 nm for ZrBTC2. The relative percentages of pore volumes for these three families of micropores were: 23% for pores of average size equal to 0.6 nm, 4.7%

for pores of average size equal to ca. 1.0 nm, and 30% for pores of average size of ca. 1.3 nm. Besides these three families of micropores, ZrBTC2 displayed a family of mesopores with an average size of ca. 6.0 nm. In contrast to what was observed for ZrBTC1, the distribution of sizes of the mesopores was narrower spanning from 2.0 to 10.5 nm. ZrBTC3 presented the lowest cumulative pore volume; namely  $0.28 \text{ cm}^3$ , implying that by using  $\text{ZrO}(\text{NO}_3)_2 \cdot x\text{H}_2\text{O}$  as precursor 61% of the pore volume is lost as compared to the use of  $\text{ZrCl}_4$ . As in the case of ZrBTC2, four families of pores were found for ZrBTC3. While the three families of micropores found for ZrBTC3 had similar average sizes as those estimated for ZrBTC2, the average size of the mesopores shifted to ca. 3.5 nm as compared to the 6.0 nm calculated for ZrBTC2. In addition, mesopore sizes spanned from 2.0 to 10 nm for ZrBTC3 hence implying a further reduction in sizes span as compared to ZrBTC1. Concerning the pore volume associated to these families of pores, the family at 0.6 nm contributed 36% to the total pore volume, whereas the families at 1.0, 1.3, and 3.5 nm contributed 7, 39, and 17%, respectively.

## 2.4. Surface Chemistry

**Table S4.** Elemental surface quantification of ZrBTC1, ZrBTC2, and ZrBTC3 materials synthesized from ZrCl<sub>4</sub>, ZrOCl<sub>2</sub>·8H<sub>2</sub>O, and ZrO(NO<sub>3</sub>)<sub>2</sub>·xH<sub>2</sub>O precursors, respectively.

Relative molar %	Sample		
	ZrBTC1	ZrBTC2	ZrBTC2
carbon	49.46	51.12	49.30
oxygen	41.84	40.27	41.77
zirconium	7.92	6.56	7.19
nitrogen	0.11	0.08	0.13
silicon	0.65	0.63	0.40
aluminum	< D.L.*	1.34	1.22
Empirical formula (surface)**	CO <sub>0.846</sub> Zr <sub>0.160</sub> N <sub>0.002</sub> Si <sub>0.013</sub>	CO <sub>0.788</sub> Zr <sub>0.128</sub> N <sub>0.002</sub> Si <sub>0.012</sub> Al <sub>0.026</sub>	CO <sub>0.847</sub> Zr <sub>0.146</sub> N <sub>0.003</sub> Si <sub>0.008</sub> Al <sub>0.025</sub>

\*D.L. = Detection Limit; \*\*Measured on a hydrogen free basis.

The nitrogen presence can be associated to the deposition of residual dimethylamine from the hydrolysis of the DMF solvent [15] (Equation S1). This is corroborated by the fact that the peak corresponding to the N 1s core level measured in XPS, see Figure S6a-c, was found within a C.I. ±0.05;2 for the mean = [400.5, 401.5] eV hence being ascribed to C-NH species [16]. Considering the hydrolysis of DMF (Equation S1) such a species can be more precisely attribute to residual dimethylamine. Given that the corresponding component of this species in the C 1s core level overlaps with the component Ar-(C-O)-Zr, Figure S6d-f, the relative concentration of C-NH was subtracted from the total relative concentration of the corresponding carbon component following the stoichiometry of dimethylamine.

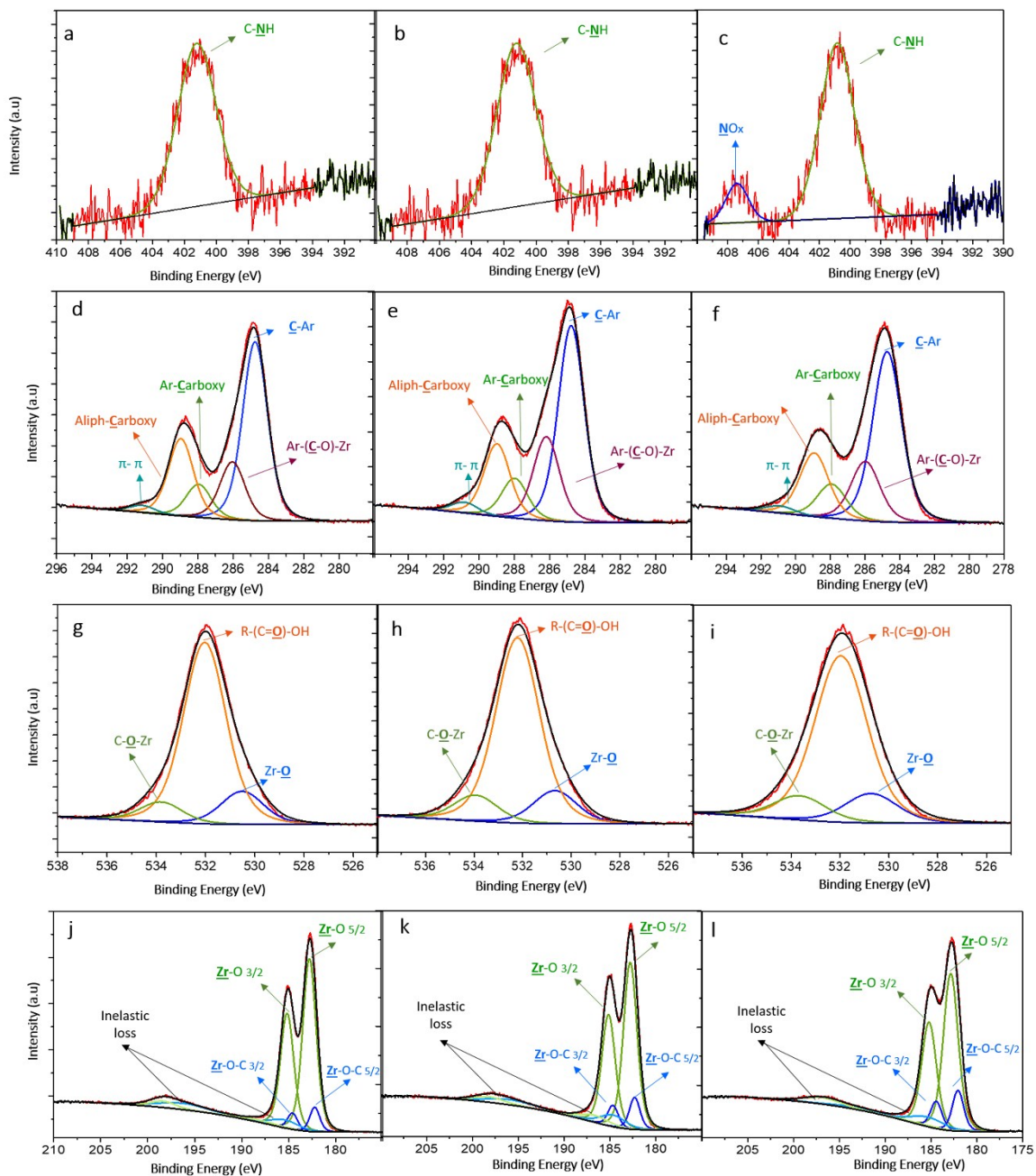
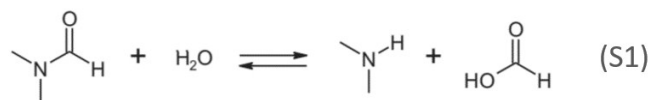


**Figure S6.** N 1s, C 1s, O 1s and Zr 3d peaks decomposition recorded in XPS analysis of ZrBTC MOFs from precursors: (a,d,g,j)  $\text{ZrCl}_4$  (ZrBTC1), (b,e,h,k)  $\text{ZrOCl}_2 \cdot 8\text{H}_2\text{O}$  (ZrBTC2) and (c,f,i,l)  $\text{ZrO}(\text{NO}_3)_2 \cdot x\text{H}_2\text{O}$  (ZrBTC3). The C-(C,H) component at 284.8 eV was taken as reference for the binding energy calibration.

Concerning silicon and aluminum, their presence can be related to the impurities of the precursors salts themselves or, in the case of silicon, to Silicone contamination from sample handling and storage in conventional desiccators. [17]. The Si 2p and Al 2p peaks recorded in XPS are shown in Figure S7. The General Spectra of the three synthesized materials is showed in Figure S8.

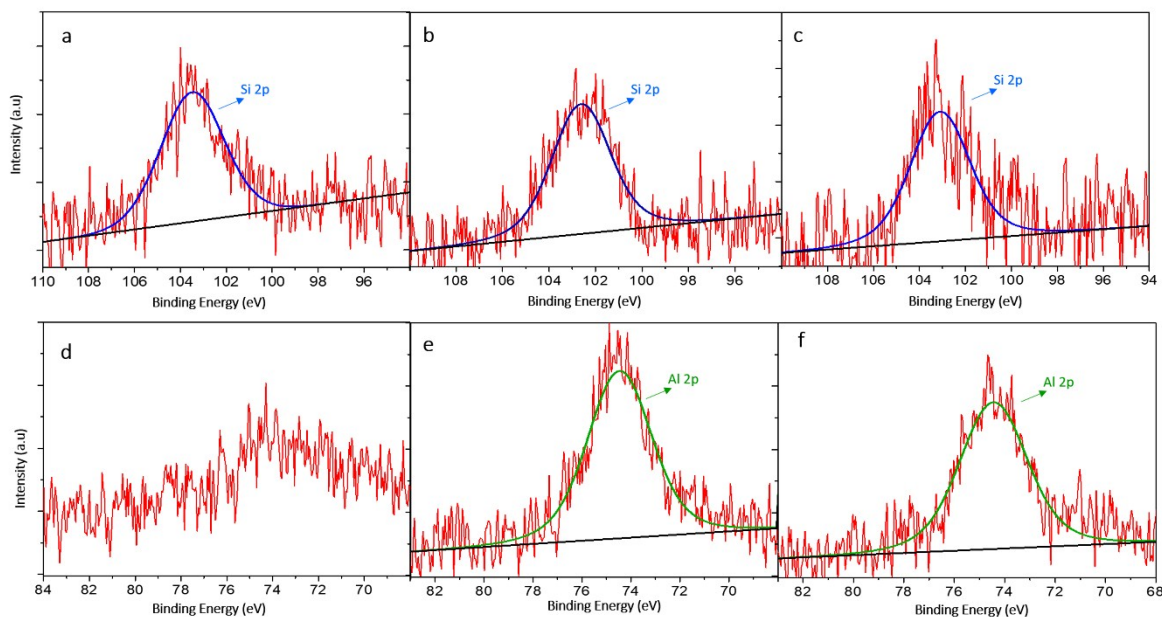


**Figure S7.** Si 2p and Al 2p peaks recorded in XPS analysis of ZrBTC MOFs from precursors: (a,d)  $\text{ZrCl}_4$  (ZrBTC1), (b,e,)  $\text{ZrOCl}_2 \cdot 8\text{H}_2\text{O}$  (ZrBTC2) and (c,f)  $\text{ZrO}(\text{NO}_3)_2 \cdot x\text{H}_2\text{O}$  (ZrBTC3). The C-(C,H) component at 284.8 eV was taken as reference for the binding energy calibration.

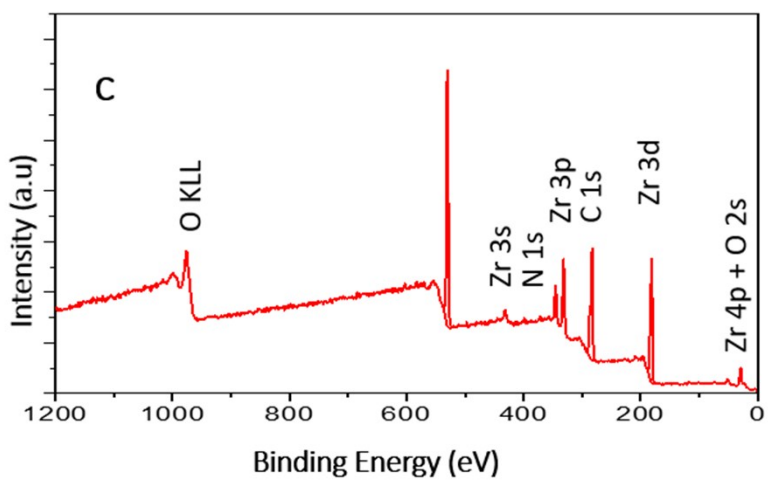
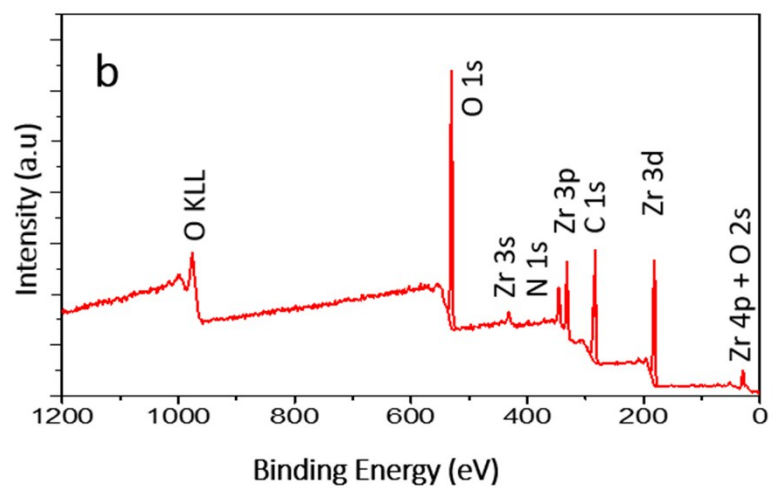
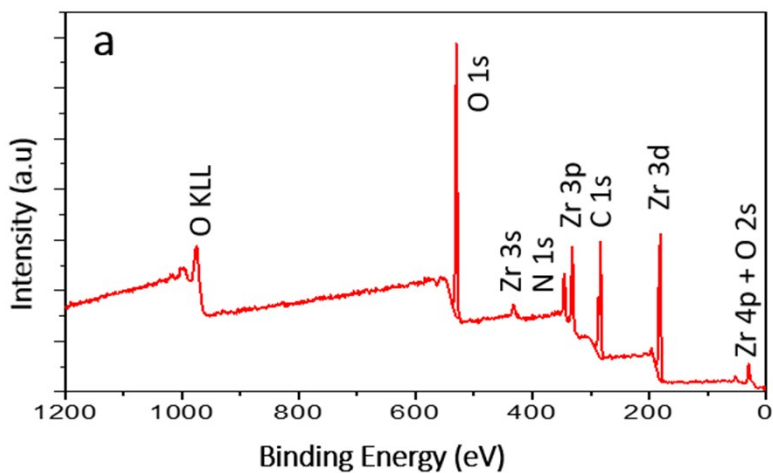


**Figure S8.** General spectra recorded in XPS analysis of ZrBTC MOFs from precursors: (a)  $\text{ZrCl}_4$  (ZrBTC1), (b)  $\text{ZrOCl}_2 \cdot 8\text{H}_2\text{O}$  (ZrBTC2) and (c)  $\text{ZrO}(\text{NO}_3)_2 \cdot x\text{H}_2\text{O}$  (ZrBTC3). The C-(C,H) component at 284.8 eV was taken as reference for the binding energy calibration.

### Supplementary References

1. Liu, S., et al., *Fast Syntheses of MOFs Using Nanosized Zeolite Crystal Seeds In Situ Generated from Microsized Zeolites*. *Crystal Growth & Design*, 2013. **13**(7): p. 2697-2702.
2. Moellmer, J., et al., *Insights on Adsorption Characterization of Metal-Organic Frameworks: A Benchmark Study on the Novel soc-MOF*. *Microporous and Mesoporous Materials*, 2010. **129**(3): p. 345-353.
3. Kaskel, S., *The chemistry of metal-organic frameworks: synthesis, characterization, and applications*. 2016: John Wiley & Sons.
4. Barrett, E.P., L.G. Joyner, and P.P. Halenda, *The Determination of Pore Volume and Area Distributions in Porous Substances. I. Computations from Nitrogen Isotherms*. *Journal of the American Chemical Society*, 1951. **73**(1): p. 373-380.
5. Walton, J., et al., *Film thickness measurement and contamination layer correction for quantitative XPS*. *Surface and Interface Analysis*, 2016. **48**(3): p. 164-172.
6. Rouxhet, P.G. and M.J. Genet, *XPS analysis of bio-organic systems*. *Surface and Interface Analysis*, 2011. **43**(12): p. 1453-1470.
7. Genet, M.J., C.C. Dupont-Gillain, and P.G. Rouxhet, *XPS analysis of biosystems and biomaterials*, 2008, Springer. p. 177-307.
8. Briggs, D. and G. Beamson, *Primary and secondary oxygen-induced C1s binding energy shifts in x-ray photoelectron spectroscopy of polymers*. *Analytical Chemistry*, 1992. **64**(15): p. 1729-1736.

9. Moulder, J.F., J. Chastain, and R.C. King, *Handbook of X-ray Photoelectron Spectroscopy: A Reference Book of Standard Spectra for Identification and Interpretation of XPS Data*. 1995: Physical Electronics.
10. Rouquerol, J., P. Llewellyn, and F. Rouquerol, *Is the bet equation applicable to microporous adsorbents?*, in *Studies in Surface Science and Catalysis*, P.L. Llewellyn, et al., Editors. 2007, Elsevier. p. 49-56.
11. Condon, J.B., *Surface area and porosity determinations by physisorption: measurements and theory*. 2006: Elsevier.
12. Wißmann, G., et al., *Modulated synthesis of Zr-fumarate MOF*. *Microporous and Mesoporous Materials*, 2012. **152**: p. 64-70.
13. *NIST X-ray Photoelectron Spectroscopy Database, NIST Standard Reference Database Number 20, National Institute of Standards and Technology, Gaithersburg MD, 20899 (2000)*. August 15th 2018]; Available from: <https://srdata.nist.gov/xps/Default.aspx>.
14. Aguié-Béghin, V., et al., *Structure and Chemical Composition of Layers Adsorbed at Interfaces with Champagne*. *Journal of Agricultural and Food Chemistry*, 2009. **57**(21): p. 10399-10407.